

About the Optimal Grid for SMOS Level 1C and Level 2 Products

M. Talone, *Member, IEEE*, M. Portabella, J. Martínez, and V. González-Gambau

Abstract—Remotely sensed measurements acquired by the European Space Agency's Soil Moisture and Ocean Salinity (SMOS) satellite are processed in a uniform equal-area grid, the Icosahedral Snyder Equal Area (ISEA) 4H9. Brightness temperature measurements are projected onto that grid (the so-called Level 1C), as well as sea surface salinity and soil moisture estimates (Level 2). The ISEA grid has been chosen for its characteristics of equal area and almost uniform intercell spacing. Nevertheless, when considering the SMOS viewing geometry, the measurement footprint size, and the processing applied to those measurements, this choice may be revisited. With this objective, the ISEA 4H9 grid is compared to other equal-area grids with different sizes and orientations with respect to the satellite track. The best configuration resulted to be a 25-km-width grid symmetrical with respect to satellite track. This grid appeared to be better suited for improving SMOS Level 2 retrieval algorithms as well as to serve as input for higher level data production, since it best accounts for the instrument's viewing geometry and substantially reduces the correlation between adjacent grid cells.

Index Terms—Grid, Icosahedral Snyder Equal Area (ISEA), Soil Moisture and Ocean Salinity (SMOS).

I. INTRODUCTION AND RATIONALE

THE European Space Agency (ESA)'s Soil Moisture and Ocean Salinity (SMOS) satellite is the first satellite embarking a 2-D interferometric radiometer [1], [2]. SMOS' unique payload is the Microwave Imaging Radiometer by Aperture Synthesis (MIRAS) [2], a 2-D L-band interferometric radiometer consisting of 69 antennas uniformly distributed in a Y-shaped array. Due to the particular geometry of MIRAS, SMOS's field of view (FOV) has the form of a distorted hexagon [3]. Several parameters vary within the FOV for a single snapshot, among them the incidence angle (0° – 65°), the spatial resolution (from 30 to 100 km, depending on the pixel position), and the radiometric accuracy and sensitivity (approximately 1.3 K standard deviation over the FOV and from 1.8 to 4.5 K, respectively, depending on the position of the pixel in the FOV [4]).

Manuscript received February 26, 2014; revised August 26, 2014 and February 11, 2015; accepted March 19, 2015. This work was supported by the Spanish Ministry of Economy and Competitiveness under the Projects MIDAS-7 AYA2012-39356-C05-03. This work was also performed within the framework of the European Union Cooperation in Science and Technology (COST) Action ES1001 SMOS Mission Oceanographic Data Exploitation.

M. Talone is with Soil Moisture and Ocean Salinity—Barcelona Expert Centre (SMOS-BEC), 08003 Barcelona, Spain, and also with the Institute for Environment and Sustainability of the European Commission Joint Research Centre (IES-JRC), 21027 Ispra, Italy (e-mail: marco.talone@jrc.ec.europa.eu).

M. Portabella, J. Martínez, and V. González-Gambau are with Soil Moisture and Ocean Salinity—Barcelona Expert Centre (SMOS-BEC), 08003 Barcelona, Spain.

Digital Object Identifier 10.1109/LGRS.2015.2416920

At every snapshot, MIRAS' 69 antennas collect the radiation coming from the Earth surface and generate a set of "visibilities." Brightness temperatures are calculated from the cross-correlation of these visibilities. The result is an image of the brightness temperatures acquired at the antenna frame and expressed in the cosine domain (ξ, η) .¹ At this point, the brightness temperatures are projected from the antenna frame onto the Earth surface. All of the projected measurements of the same half-orbit (from pole to pole) constitute the Level 1C (L1C) product. Starting from the L1C product, the SMOS Level 2 (L2) processor generates an L2 product, i.e., geophysical estimates in a single satellite overpass. For every grid cell, several brightness temperature observations belonging to different snapshots and with different incidence angles (sum of θ and φ in¹) and radiometric characteristics are used to produce a single soil moisture (SM) or sea surface salinity (SSS) estimate. The number of brightness temperatures used depends on the across-track position of the grid cell; the set of L1 measurements needed to produce an L2 estimate is referred to as dwell-line. SSSs and SMs are retrieved following a Bayesian approach, minimizing a cost function that includes both remote-sensing observations and auxiliary *a priori* information. Additional products are generated based on the Level 2 data but with different grids, by spatiotemporal average/optimal interpolation of these data (Level 3 products), while Level 4 products consist of derived geophysical parameters obtained using SMOS data jointly with external information.

SMOS' L1C and L2 products are distributed in the Icosahedral Snyder Equal Area (ISEA) 4H9 grid [5], [6]. The ISEA 4H9 grid is a hexagonal equal-area grid characterized by an almost constant intercell distance of approximately 15 km (half of the size of the smallest SMOS measurement).

The objective of this study is to demonstrate that the SMOS grid can be improved both in orientation and size, leading to a lower cross-correlation between adjacent measurements. The independence of the measurements is, in fact, among the most critical parameters affecting the quality of both the retrieval at Level 2 and the exploitation of the data at Levels 3 and 4. The Bayesian algorithm for retrieving SM/SSS at Level 2 is based on the assumption of independence among the measurements of the same dwell-line; likewise, the optimal interpolation procedures applied at Level 3 and 4 take for granted the independence of the error of contiguous grid cells.

Considering the instrument geometry and the particular retrieval algorithm applied for SMOS, an optimal grid should ensure the best correspondence between measurement footprint

¹ $(\xi, \eta) = (\sin(\theta) \cos(\varphi), \sin(\theta) \sin(\varphi))$, where θ is the angle from the normal to the instrument plane ($0 \leq \theta \leq \pi/2$) and φ is the angle in the instrumental plane ($0 \leq \varphi \leq \pi/2$) [2].

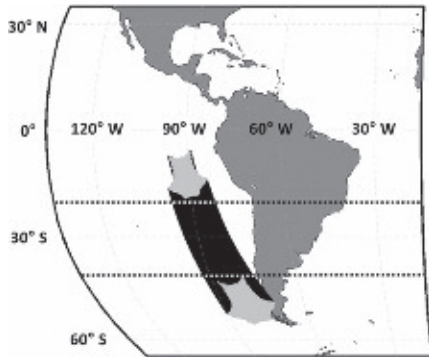


Fig. 1. Entire set of snapshots used in the study. The horizontal dotted lines identify a zone devoid of artifacts.

and grid cell, in terms of the following: 1) the minimum overlap of measurement footprints per grid cell; 2) the minimum presence of uncovered areas; and 3) a maximum correspondence between the original and projected measurements, i.e., a ratio between the area of the measurement footprint and the area of the grid cell tending to 1. At the same time, it should provide 4) the minimum overlap among measurements belonging to the same dwell-line (acquired in different snapshots). Finally, considering the need of monitoring the status of the instrument to detect possible drifts or malfunctioning (for calibration and validation purposes), 5) the level of homogeneity of the instrumental characteristics along a dwell-line should be taken into account in the selection of an optimal grid.

To test these characteristics, a set of snapshots has been simulated, and the independent brightness temperature has been projected onto different grids to be compared with the currently used ISEA 4H9.

The data and tools used to set up the experiment are presented in Section II. The methodology followed to define the best orientation and size as well as the results obtained are described in Section III. Finally, the main conclusion is drawn in Section IV.

II. DATA AND TOOLS

To assess the quality of the current SMOS grid, a total of 500 snapshots have been simulated, observing at ground an area in the Pacific Ocean framed between 55°S and 5°S in latitude and 100°W and 70°W in longitude. For computational reasons, the study has been restricted to the part of the semiorbit centered on the South Pacific subtropical region. However, the conclusions can be extended to the entire semiorbit since the area of the grid cell does not change with latitude, and the change of the SMOS' FOV, only due to the change of the curvature of the Earth and of the distance satellite–Earth, can be considered negligible. The entire zone of interest is shown in Fig. 1, where the first and last snapshots are highlighted in light gray. The two horizontal dotted lines identify the latitude boundaries (between 20°S and 40°S) used to calculate the statistics in Section III; this is, in fact, free from the artifact transition areas at the beginning and end of the track.

As mentioned in the introduction, for each snapshot, independent brightness temperature measurements are generated in the antenna frame from the cross-correlation of the measurements of the different antennas (visibilities). The visibilities

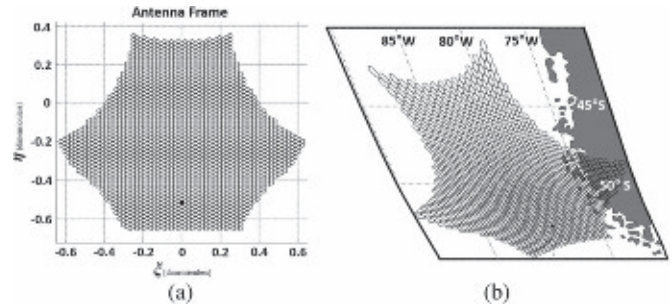


Fig. 2. Independent SMOS measurements (a) in the antenna frame and (b) projected onto the Earth map according to a Robinson projection.

can be transformed into brightness temperature by a sort of bidimensional Fourier transformation, applying the so-called G-matrix [7]; the difference between the ideal Fourier transformation and the G matrix is that the latter accounts for the actual differences in the antenna patterns of the 69 antennas as well as for the correlation of the receptor filters. The lowest resolution to transform visibilities into brightness temperatures is set by the instrument characteristics and given by $(N_T \times N_T)$, with $N_T = 3 \cdot N_{EL} + 1$, where N_{EL} is the number of element per arms (21) [4]. Using a resolution of (64×64) points ensures the maximum independence among measurements of the same snapshot. The obtained brightness temperatures are projected onto the ground using ESA's Earth Observation Customer Furnished Item (EOCFI) [8] Orbit Propagation libraries and the official auxiliary files used in the SMOS Data Product Generation Center (DPGS) [9].

An example of the independent measurements in the antenna frame and their projection onto the Earth map (according to a Robinson projection) are shown in Fig. 2(a) and (b), respectively.

As it can be noticed, the projection strongly distorts the measurement dimension [Fig. 2(b)]; this distortion is proportional to the distance from the boresight (black dot at $(\xi, \eta) = (0, -0.52)$). In particular, the measurements at the border of the FOV, i.e., those at the far right and left, and at the top of the FOV, can reach 50–100 km of width in the longer dimension, respectively.

Once projected, the measurements are split according to the projection grid; the following three different types of grids are compared.

- 1) ISEA: In its version 4H9, it is the currently used grid for SMOS L1C and L2 products; the area of each cell is constant, while the distance between the centers of two adjacent cells slightly varies around 15 km (4H9).
- 2) A constantly spaced (15 km) uniform grid, with no symmetry with respect to the satellite track.
- 3) A constantly spaced (15 km) uniform grid, symmetric with respect to the satellite track

In Fig. 3(a)–(c), one of FOVs is shown as an example; grids A, B, and C are superimposed, respectively. To avoid confusions, throughout this letter, the circular/elliptical measurements will be simply called footprints, while the hexagonal/square/rhomboid cells on ground will be referred to as grid cells.

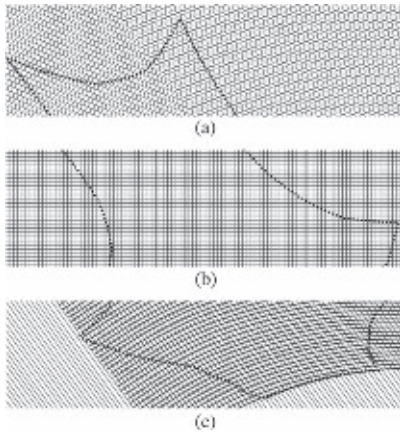


Fig. 3. Example of intersection between SMOS' FOV and (a) ISEA 4H9, (b) grid B (25 km), and (c) grid C (25 km).

III. METHODOLOGY AND DISCUSSION

SMOS, in its current configuration, operates in full-polarimetric mode—all of the four Stokes parameters are acquired every four snapshots (the measurement strategy is quite complex and is illustrated in [10]); however, for simplicity, polarizations are considered separately, and only the case of X-pol is analyzed, which implies using only one every four snapshots. The results and conclusions drawn in this study obviously apply as well to the other SMOS polarizations.

A. Grid Type

MIRAS' major features are strongly dependent on the viewing geometry and, in particular, on the across-swath position [5], including the radiometric sensitivity, spatial resolution, and angular coverage. As a consequence of that, the SM/SSS retrieval itself is highly connected to the across-swath position of the grid cell. This is a typical characteristic of many satellite remote sensing instruments with swath-viewing capabilities (e.g., push-broom polar orbiters), such as the scatterometers onboard the European Remote Sensing satellite [11], [12] and the MetOp series [13] as well as the Sea-Viewing Wide FOV Sensor (SeaWiFS) on the OrbView-2 satellite (at Level 2) [14], among others. In such cases, a nonfixed grid symmetrical with respect to the satellite track has been chosen and proven to be very useful for the improvement of the Level 2 algorithms, simplifying the characterization of the errors, the optimization of the inversion, and the quality control and calibration of the measurements [15], [16].

To assess the effect of using different grids, the misalignment between the actual footprint location and the grid cell has been calculated as the standard deviation of the across-track position inside three 25-km-wide strips centered at the boresight, at the middle, and at the edge of the FOV, respectively (Fig. 4). This has been computed for the ISEA 4H9 grid, the 15-km uniform square grid, and the 15-km grid symmetrical to the satellite track. The choice of a width of 25 km guarantees the absence of along-track holes due to the misalignment between grids and strips.

Results are shown in Table I, in terms of standard deviation in the cosine domain (ξ) as well as its equivalent in kilometers. This depends on the along-track position of the grid cell inside

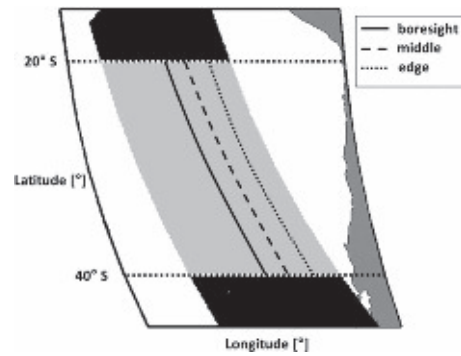


Fig. 4. Three 25-km-wide strips at constant across-track position. The solid line is at boresight, the dashed line is at the middle of the FOV, and the dotted line is at the edge of the FOV.

TABLE I
MISALIGNMENT BETWEEN FOOTPRINT AND GRID CELL LOCATIONS

ξ [10^{-3}](dimensionless) / [min,max] km	Grid A	Grid B	Grid C
Boresight	10.2 / [8, 13]	6.0 / [5, 8]	4.7 / [4, 6]
Middle of the FOV	16.3 / [13, 22]	8.9 / [7, 12]	5.6 / [4, 7]
Edge of the FOV	20.8 / [16, 23]	5.9 / [5, 7]	3.4 / [3, 4]

the FOV; its minimum and maximum values are reported in brackets.

The standard deviation of the across-track position (both in terms of ξ and in kilometers) decreases by a factor of 2–6 (maximum on the edge of the FOV) using grid C instead of the currently used grid A.

B. Grid Size

Considering the impact of the Level 2 grid on the quality of the higher level products (Level 3 and Level 4), the oversampling introduces substantial correlation between adjacent grid cells. In optimal interpolation and data assimilation in general, a Bayesian-based cost function is minimized. This cost function has two terms: the observational term and the background term, which include the inverse of the observation error covariance matrix O and the inverse of the background error covariance matrix B , respectively. Background error cross-correlations (error correlations between adjacent cells), i.e., off-diagonal terms, are estimated and used in the minimization (these are needed to cope with the inherent underdetermination of the data assimilation, i.e., much less observations than grid cells and parameters to be resolved). Observation error cross-correlations are very difficult to estimate, and as such, off-diagonal terms in the O matrix are not considered (set to zero). In data assimilation, many observations are removed (thinning) to avoid observation error correlations (between adjacent cells). The footprint overlapping introduces measurement error cross-correlations, which are usually not taken into account, leading to lower quality L3 OI maps. If taken into account (i.e., by thinning), a substantially lower amount of measurements will be used, which will also negatively impact the quality of the OI maps. By reducing or removing measurement error cross-correlations, it is possible to maximize the amount of measurements available, therefore optimizing the impact on L3 OI maps quality [17].

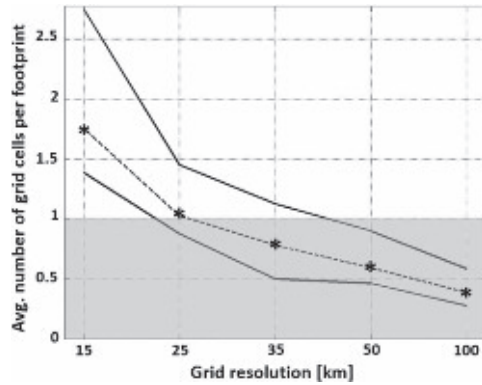


Fig. 5. Average number of grid cells per footprint using grid C and considering different grid sizes from 15 to 100 km. The dashed line represents the average value, while the solid lines are the maximum and minimum values.

TABLE II
AVERAGE PERFORMANCE AS A FUNCTION OF THE GRID CELL AREA

Min – Avg – Max	Grid cells per footprint	Avg. area used per footprint / grid-cell area
15 km	1.39 - 1.75 - 2.75	1.74 - 2.54 - 3.62
25 km	0.88 - 1.03 - 1.45	0.65 - 0.90 - 1.30
35 km	0.50 - 0.78 - 1.12	0.33 - 0.45 - 0.66
50 km	0.46 - 0.59 - 0.90	0.16 - 0.22 - 0.32
100 km	0.27 - 0.39 - 0.59	0.05 - 0.08 - 0.12

To minimize the oversampling, different grid sizes have been compared. A preliminary test to roughly determine the optimal grid size (once chosen grid C after the grid-type evaluation) has been performed: the minimum, the average, and the maximum number of grid cells per footprint have been calculated using an equispaced grid, with grid sizes of 15, 25, 35, 50, and 100 km. These grids are shown in Fig. 5, where the dashed line represents the average value, while the solid lines are the maximum and minimum values.

The threshold of a single grid cell per measurement is highlighted in gray. All of the figures have been obtained considering only the zone bound in latitude between 20°S and 40°S and discarding those footprints intersecting the relative grid cell with less than 5% of their area.

The same values are shown in Table II, along with the ratio between the average area used per footprint and the grid cell area.

Considering the global performances (Fig. 5 and Table II), when using a 15-km-wide grid, the average number of grid cells sharing the same footprint is always higher than 1 and ranges between 1.39 and 2.75; taking into account the areas of the footprint and of the grid cell, for each measurement, 2.54 times the grid cell area is used on average. As expected, the curves decrease when the grid size increases and reach their value closest to one when the grid size is 25 km (with a ratio between the footprint and the grid cell areas of 0.9). Hence, according to Fig. 5 and Table II, to minimize the overlapping of the footprints and at the same time fulfill the requirement of one grid cell per measurement, a grid of around 25 km should be chosen.

However, due the high variability of the geometric and radiometric features of the SMOS measurements, a more detailed analysis must be performed. The average number of grid cells per footprint has been analyzed as a function of the incidence angle—over the dwell-line—and as a function of the across-

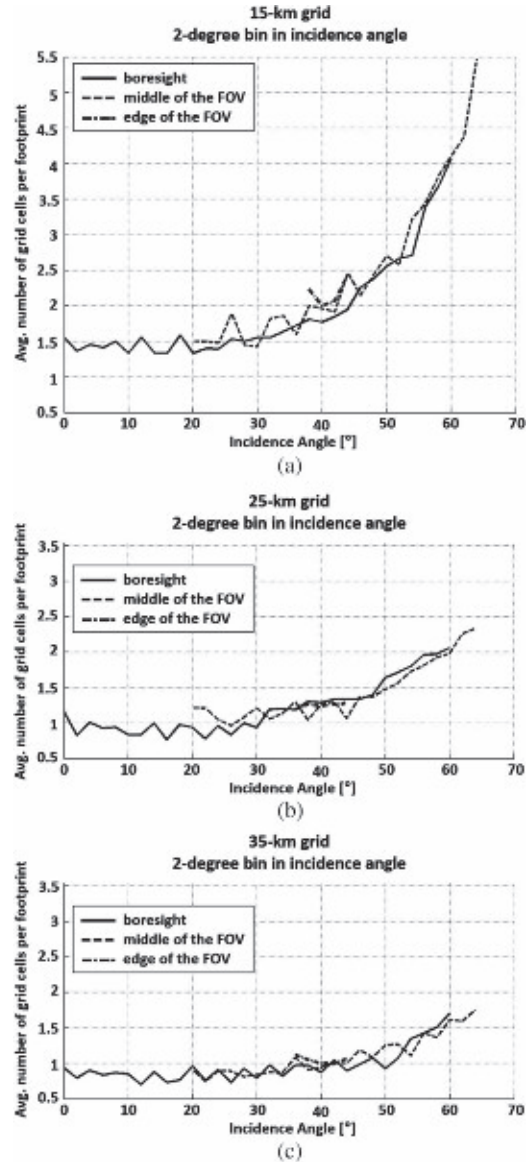


Fig. 6. Average number of grid cells sharing the same footprint as a function of the incidence angle for a certain grid cell. Solid lines indicate that the grid cell is at the boresight, dashed lines indicate that it is at the middle of the FOV, and dotted lines indicate that it is at the edge of the FOV.

track position. For convenience, the grid size range has been restrained to the 15–35-km range. The results for the first analysis—over the dwell-line—are shown in Fig. 6(a) (15 km), (b) (25 km), and (c) (35 km), where the average number of grid cells sharing the same footprint, calculated over 2° bins, is plotted as a function of the incidence angle for certain across-swath positions. Note that only the intersections involving more than 95% of the grid cell area have been considered. As in Fig. 4, the solid line indicates the grid cells at the boresight (nadir), the dashed line indicates the middle of the FOV, and the dotted line indicates the edge of the FOV.

Using a grid of 15 km, the same footprint is shared by approximately 1.5 grid cells up to 30°, when this number rapidly increases up to 5. Lower values are found for points at the boresight, while at the middle of the FOV, it is always higher than 1.5. Note that very few measurements are available at the edge of the FOV, all around 40° incidence angle and shared

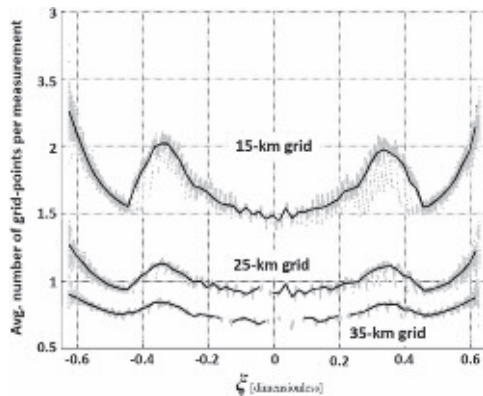


Fig. 7. Average number of grid cells sharing the same footprint as a function of cross-track position (ξ). Solid lines are the average values calculated in bins of 0.02 in the ξ -axis.

by two grid cells (at 15-km grid size). When the grid size is increased to 25 km, the slope of the curve substantially decreases, as well as its mean value. The average number of grid cells sharing the same footprint is mostly between 0.9 and 1.5 up to 50° , with the lowest values for the cells at the boresight. For the cells located at the middle of the FOV, this number is almost constant at 1.2 between 20° and 50° and reaches 2 at 60° . For the cells at the edge of the FOV, it is around 1.2. Considering the last grid size (35 km), the average number of grid cells sharing the same footprint is lower than 1 up to 40° for all of the cells and then slowly increases up to 1.7 at 60° . According to these results, 25 km is confirmed as the optimal grid cell size.

The last test, designed to highlight the effect of the across-track position, consists of compressing the along-track dimension all over the artifact-free area (i.e., between the horizontal dotted lines in Fig. 4). The result is shown in Fig. 7, where the mean value of the average number of grid cells per footprint is plotted as a function of the across-track position (ξ); the dots indicate the average number of grid cells per measurement, while the solid line indicates its average value per bins of 0.02 in the ξ -axis.

As it can be noticed, the main pattern is similar for different grid sizes, due to its high correlation with the number of measurements. However, the amplitude of the oscillation and the mean value are substantially reduced when the grid size increases. For the 15-km-wide grid, the mean value is approximately 1.75 ± 0.25 , which becomes 1 ± 0.1 for a grid of 25 km and 0.75 ± 0.1 for a grid of 35 km.

In summary, considering both the global performance and also the behavior as a function of the incidence angle and the across-track position, the 25-km grid seems to represent the optimal grid size, being a tradeoff between minimizing the overlap between adjacent grid cells and preventing the presence of gaps in the retrieved SSS/SM field. Among the possible different orientations of the grid, keeping symmetry to the satellite track (i.e., a grid dependent on observation geometry) will help in detecting data processing issues (related to, for example, calibration, error characterization, inversion, quality control, monitoring, etc.), thus contributing to the geophysical retrieval quality improvement and, in general, to the instrument calibration and validation activities.

IV. CONCLUSION

With the objective of improving the SMOS L1C–L2 grid (currently the ISEA 4H9), various grid types and sizes have been evaluated. Similar to other satellite remote sensing missions, a 25-km-wide equal-area grid symmetrical with respect to the satellite track is shown to best fit the SMOS viewing geometry and footprint sizes, and therefore, it is optimal for validation and geophysical retrieval purposes. Moreover, such grid is also convenient for data assimilation and higher level data production (L3 and L4) since it substantially reduces spatial correlation between adjacent grid cells, contributing to the improvement of the quality of the products. As a final remark, it must be mentioned that only the signal received by the main lobe (90% of the total) has been considered for this study and that the inclusion of the signal received by secondary lobes could increase the correlation among neighbor grid cells and lead to a further enlargement of the optimal grid.

REFERENCES

- [1] Y. H. Kerr *et al.*, "The SMOS mission: New tool for monitoring key elements of the global water cycle," *Proc. IEEE*, vol. 98, no. 5, pp. 666–687, May 2010.
- [2] K. D. McMullan *et al.*, "SMOS: The payload," *IEEE Trans. Geosci. Remote Sens.*, vol. 46, no. 3, pp. 594–605, Mar. 2008.
- [3] A. Camps, B. Javier, I. Corbella, and F. Torres, "The processing of hexagonally sampled signals with standard rectangular techniques: Application to 2-D large aperture synthesis interferometric radiometers," *IEEE Trans. Geosci. Remote Sens.*, vol. 35, no. 1, pp. 183–190, Jan. 1997.
- [4] I. Corbella *et al.*, "MIRAS calibration and performance: Results from the SMOS in-orbit commissioning phase," *IEEE Trans. Geosci. Remote Sens.*, vol. 49, no. 9, pp. 3147–3155, Sep. 2011.
- [5] J. P. Snyder, "An equal-area map projection for polyhedral globes," *Cartographica*, vol. 29, no. 1, pp. 10–21, Spring 1992.
- [6] M. Suess, P. Matos, A. Gutierrez, M. Zundo, and M. Martin-Neira, "Processing of SMOS Level 1C data onto a discrete global grid," in *Proc. IEEE IGARSS*, 2004, 1914–1917.
- [7] I. Corbella, F. Torres, A. Camps, N. Duffo, and M. Vall-llossera, "Brightness temperature retrieval methods in synthetic aperture radiometers," *IEEE Trans. Geosci. Remote Sens.*, vol. 47, no. 1, pp. 285–294, Jan. 2009.
- [8] EOCCI Website. [Online]. Available: <http://eop-cfi.esa.int/index.php/mission-cfi-software/eocfi-software>
- [9] SMOS Level 1 and Auxiliary Data Products Specifications—SO-TN-IDR-GS-0005. [Online]. Available: www.smos.com.pt/project_docs.html
- [10] M. Martín-Neira, S. Ribo, and J. A. Martín-Polegre, "Polarimetric mode of MIRAS," *IEEE Trans. Geosci. Remote Sens.*, vol. 40, no. 8, pp. 1755–1768, Aug. 2002.
- [11] P. Lecomte, "The ERS scatterometer instrument and the on-ground processing of its data," presented at the Proc. Emerging Scatterometer Appl.—From Research Operations, Noordwijk, The Netherlands, Oct. 5–7, 1998, Paper ESA-SP-424.
- [12] R. Crapolicchio *et al.*, "ERS-2 scatterometer: Mission performances and current processing achievements," *IEEE Trans. Geosci. Remote Sens.*, vol. 50, no. 7, pp. 2427–2448, Jul. 2012.
- [13] ASCAT Product Guide—EUM/OPS-EPS/MAN/04/0028. [Online]. Available: www.eumetsat.int
- [14] SeaWiFS Level-2 Product Specifications. [Online]. Available: http://oceancolor.gsfc.nasa.gov/DOCS/Ocean_Level-2_Data_Products.pdf
- [15] ERS Scatterometer Cyclic Reports. [Online]. Available: http://earth.esa.int/pcs/ers/scatt/reports/pcs_cyclic/
- [16] C. Anderson *et al.*, "Validation of backscatter measurements from the Advanced Scatterometer on MetOp-A," *J. Atmos. Ocean. Technol.*, vol. 29, no. 1, pp. 77–88, Jan. 2012.
- [17] Z.-Q. Liu and F. Rabier, "The interaction between model resolution, observation resolution and observation density in data assimilation: A one-dimensional study," *Q. J. R. Meteorol. Soc.*, vol. 128, no. 582, pp. 1367–1386, Apr. 2002.